Measurement report: Size-resolved and seasonal variations in aerosol hygroscopicity dominated by organic formation and aging: Insights from a year-long observation in Nanjing

Junhui Zhang[1], Yuying Wang[1], Jialu Xu[1], Xiaofan Zuo[1], Chunsong Lu[1], Bin Zhu[1], Yuanjian Yang[1], Xing Yan[2], Yele Sun[3]

[1]State Key Laboratory of Climate System Prediction and Risk Management/Key Laboratory for Aerosol–Cloud Precipitation of China Meteorological Administration/Special Test Field of National Integrated Meteorological Observation, Nanjing University of Information Science & Technology, Nanjing 210044, China
[2]Faculty of Geographical Science, Beijing Normal University, Beijing 100875, China
[3]State Key Laboratory of Atmospheric Environment and Extreme Meteorology, Institute of Atmospheric Physics, Chinese Academy of Sciences, Beijing 100029, China

Correspondence to: Yuying Wang (yuyingwang@nuist.edu.cn)

Abstract: Aerosol hygroscopicity plays a significant role in atmospheric chemistry, radiation, and climate effects. While previous studies have investigated regional differences in aerosol hygroscopicity, long-term observational studies focusing on seasonal variations in specific regions remain scarce. This study explores size-resolved and seasonal variations in aerosol hygroscopicity in northern Nanjing, using one-year hygroscopicity-tandem differential mobility analyser (H-TDMA) measurements in 2021. Aerosols in the region show relatively low hygroscopicity due to a high organic content (annual average mass fraction: 42.92% in $PM_{2.5}$) in fine particles. The mean hygroscopicity parameter (κ_{mean}) increases with particle size across all seasons. Particles (40–200 nm) show seasonal κ_{mean} variations: winter (0.12–0.24) and spring (0.14–0.25) display relatively higher values attributable to relatively higher secondary inorganic content, while summer (0.12–0.21) and autumn (0.10–0.20) exhibit relatively weaker hygroscopicity due to enhanced contributions from less hygroscopic components. Diurnal patterns are shaped by photochemical aging and aqueous-phase reactions, leading to κ_{mean} slight enhancement for larger particles in the afternoon and evening. New particle formation (NPF) events occur most frequently in spring. During spring NPF days, Aitken-mode particles exhibit slightly low hygroscopicity, whereas accumulation-mode particles demonstrate relatively higher hygroscopicity compared to non-NPF days. Regional transport analysis reveals distinct controlling factors: hygroscopicity of 40 nm particles may be mainly controlled by local sources, while 200 nm particles are more influenced by seasonal air mass transport. These results improve understanding of aerosol–cloud interactions and support regional climate modeling and air quality management in urbanizing areas.

1. Introduction

Aerosols, defined as mixtures of solid and liquid particles suspended in the air, possess hygroscopicity as a fundamental physicochemical property that governs their interactions with water vapor under varying environmental relative humidity (RH). The hygroscopicity of aerosols describes their capacity to absorb water vapor, significantly influencing both the atmospheric environment and global climate through complex physicochemical processes (Chen et al., 2019; Zhang et al., 2023).

Aerosol hygroscopicity plays a central role in determining the phase state, chemical reactions, optical properties, and cloud nucleation activity of aerosol particles, thereby significantly influencing atmospheric chemistry, radiation, and climate effects (Chen et al., 2022; Peng et al., 2020; Ray et al., 2023; Swietlicki et al., 1999; Y. Wang et al., 2025; Zhang et al., 2023). Hygroscopic growth notably alters aerosol optical properties by modifying particle size distribution and refractive index, enhancing light scattering coefficient (Liu et al., 2022; Song et al., 2023). Furthermore, hygroscopicity promotes cloud formation by activating particles as cloud condensation nuclei, which leads to substantial changes in radiative forcing patterns (Rosenfeld et al., 2014; Svenningsson et al., 2006). However, aerosol hygroscopicity is influenced by various factors. Variations in environmental conditions and physicochemical processes can result in divergent hygroscopic behaviors across different atmospheric environments (Gysel et al., 2007; Jiang et al., 2025; N. Wang et al., 2025).

Currently, multiple instruments and techniques are available for measuring aerosol hygroscopicity. Among the more established instruments are the hygroscopicity-tandem differential mobility analyser (H-TDMA), the cloud condensation nuclei counter (CCN_C), and the dual-nephelometer system (Chen et al., 2023; Jin et al., 2022; Song et al., 2023; Wang et al., 2017; Zhang et al., 2017). Compared to other hygroscopicity measurement instruments, the H-TDMA, which is based on measuring particle number concentration, offers distinct advantages in studying the properties of ultrafine mode particles (Wang et al., 2019). In addition to measuring the size-resolved hygroscopic growth factor (GF) of aerosols under varying relative humidity conditions, the H-TDMA can also provide insights into the mixing state of particles and reflect aerosol chemical compositions (Chen et al., 2022; X. Wang et al., 2018). According to Köhler theory, GF depends on chemical composition (Raoult effect) and particle size (Kelvin effect) (Petters and Kreidenweis, 2007). Compared with GF, hygroscopicity parameter (κ) introduced by Petters and Kreidenweis (2007) eliminates the influence of the Kelvin effect, enabling direct comparison of hygroscopicity governed by the Raoult effect across different particle sizes (Kammermann et al., 2010; Petters and Kreidenweis, 2007).

A more profound understanding of aerosol hygroscopicity is crucial for improving the predictive capability of global climate models, particularly in simulating aerosol size distributions and their scattering properties under varying humidity conditions. The size dependence of aerosol hygroscopicity exhibits significant variations across different atmospheric environments (Peng et al., 2020; Zhang et al., 2023). To better characterize the spatiotemporal evolution of aerosol hygroscopicity under diverse pollution conditions, extensive and comprehensive studies on its spatiotemporal variability are required. Furthermore, understanding the effects of atmospheric processes, including new particle formation (NPF) and haze events, on aerosol hygroscopicity across heterogeneous environmental regimes remains imperative (Chen et al., 2022).

NPF, defined as the evolution process where newly formed sub–3 nm particles grow to larger sizes, represents a significant atmospheric aerosol source capable of influencing aerosol hygroscopicity and has been observed globally (Hirshorn et al., 2022; Shen et al., 2023; Yli-Juuti et al., 2011). Generally, freshly nucleated particles exhibit lower hygroscopicity, and the hygroscopicity increases with particle aging (Asmi et al., 2010). NPF events dominated by different chemical components exert distinct impacts on aerosol hygroscopicity. Newly formed sulfate-dominated particles exhibit higher hygroscopicity, whereas organics-dominated counterparts display lower hygroscopicity (Hong et al., 2024; Ma et al., 2016). Furthermore, Liu et al. (2021) observed that on NPF events, photochemical oxidation triggered by the nucleation of volatile organic compounds generates more water-soluble organic acids, resulting in higher hygroscopicity of organic aerosols on NPF days compared to non-NPF days.

In recent years, numerous studies on aerosol hygroscopicity based on H-TDMA observation data have been conducted globally. It has been found that the probability density function of GF or κ (GF/κ-PDF) exhibits a bimodal distribution at urban sites (Shi et al., 2022; Spitieri et al., 2023; Tan et al., 2013; X. Wang et al., 2018), while at some non-urban sites, it shows a unimodal or quasi-unimodal distribution (Chen et al., 2022; Y. Wang et al., 2018). Wang et al. (2019) discovered that ultrafine-mode particles during clean periods mainly originate from nucleation events followed by growth, whereas during severe pollution periods, they predominantly come from primary emissions in urban environments. Conversely, accumulation-mode particles are primarily from primary emissions during clean periods and secondary processes during pollution periods, resulting in notable differences of aerosol hygroscopicity for different mode particles under varying pollution levels. Additionally, aerosol hygroscopicity exhibits substantial differences among air masses of varying origins. Over the Antarctic continent, dry continental air masses are reported to exhibit stronger hygroscopicity than moist marine air masses (Asmi et al., 2010). At an urban site in Beijing, seasonal hygroscopicity variations are strongly correlated with air mass source regions (Zhang et al., 2023).

Aerosol concentration and composition undergo significant variations on both temporal and spatial scales. Long-term measurements of aerosol hygroscopicity are crucial for understanding its seasonal and annual variations, as well as its impacts on visibility, atmospheric chemistry, and climate change (Peng et al., 2020). In some regions of the world, studies utilizing H-TDMA for long-term measurements of aerosol hygroscopicity have already been conducted (Alonso-Blanco et al., 2019; Fors et al., 2011; Kammermann et al., 2010; Mamali et al., 2018; Ray et al., 2023). These observations reveal that aerosol hygroscopicity is highly depending on their sources and physicochemical aging processes. In China, numerous observational experiments measuring aerosol hygroscopicity using H-TDMA have been carried out in regions such as the North China Plain (NCP), the Yangtze River Delta (YRD), and the Pearl River Delta (PRD) (Jiang et al., 2016; Jiang et al., 2025; Wang et al., 2017). However, most measurements limit to short-term field campaigns (typically 1–2 months duration), which makes it impossible to determine the seasonal variations and their influencing factors in aerosol hygroscopicity at specific locations (Fan et al., 2020).

In this study, the H-TDMA system is utilized in the northern suburbs of Nanjing to obtain size-resolved hygroscopicity observation data for submicron aerosols, covering the entire year from January to December 2021. The H-TDMA observations

enable the determination of size-resolved and seasonal variations in aerosol hygroscopicity in the Nanjing region. Furthermore, combining these data with aerosol chemical composition measurements facilitate the further analysis of influencing factors contributing to these hygroscopicity differences. This paper is structured as follows. Section 2 describes the instrumentation and the methods to data analysis. Aerosol hygroscopicity during different seasons are discussed in Sect. 3. Conclusions and summary are given in Sect. 4.

2. Experiment and data analysis

2.1. Measurement site and campaign

A comprehensive field observation experiment was conducted in the northern suburbs of Nanjing in 2021, aiming to delve deeply into the interactions among the atmosphere, aerosol, boundary layer, and cloud. The observation site is located on the campus of Nanjing University of Information Science and Technology (NUIST, 32°13′ N, 118°46′ E) in the northern suburban area of Nanjing, which is situated in the central YRD. Further details on the field campaign and measurement site are available in previous work (Song et al. 2023; Wang et al., 2016; Yang et al., 2025).

This work provides a comprehensive examination of seasonal variations in aerosol hygroscopicity and their relationship with chemical composition, based on year-round observational data collected from January to December 2021. The dataset is partitioned according to conventional meteorological seasons: winter (Jan–Feb and Dec 2021), spring (Mar–May 2021), summer (Jun–Aug 2021), and autumn (Sep–Nov 2021).

2.2. Measurements and data analysis

2.2.1. Measurement of aerosol hygroscopicity

The H-TDMA used in this study primarily consists of two differential mobility analysers (DMA, Model 3081L, TSI Inc.) and a condensation particle counter (CPC, Model 3772, TSI Inc.). The dried and neutralized aerosol sample is first passed through the first DMA, which selects monodisperse particles of specific diameters (40, 80, 110, 150, and 200 nm). Subsequently, the sample with monodisperse particles is humidified to RH=90% via a nafion humidifier. Finally, the sample is directed through the second DMA and the CPC to measure the particle number size distribution of the humidified particles.

The hygroscopic growth factor (GF) is defined as:

$$\text{GF} = \frac{D_\text{p}(\text{RH})}{D_\text{p}(\text{dry})}, \tag{1}$$

where $D_\text{p}(\text{dry})$ denotes the dry diameter of monodisperse particles selected by the first DMA before humidification, and $D_\text{p}(\text{RH})$ represents the particle diameter selected by the second DMA after humidification at RH = 90%.

The H-TDMA data can be used to compute the measured distribution function of GF for any selected $D_\text{p}(\text{dry})$ particles, which is then used to retrieve the probability distribution function of GF (GF-PDF) according to the multi-mode TDMAfit algorithm.

The hygroscopicity parameter (κ) is calculated as follows (Petters and Kreidenweis, 2007):

$$\kappa = (\text{GF}^3 - 1) \cdot [\frac{1}{\text{RH}} \exp(\frac{4\,\sigma_{s/a}\,M_w}{R\,T\,\rho_w\,D_p\,\text{GF}}) - 1], \qquad (2)$$

where $\sigma_{s/a}$ is the surface tension of the droplet–air interface at the composition of the droplet, M_w is the molar mass of water, R is the universal gas constant, T is the temperature, and ρ_w is the density of water.

The probability distribution function of κ (κ-PDF, $c\,(\kappa, D_p)$) derived from GF-PDF is normalized by $\int c\,(\kappa, D_p)\,\mathrm{d}\kappa = 1$. Based on the κ values, aerosol particles are categorized into three hygroscopic groups: nearly hydrophobic (NH, $\kappa < 0.1$), less hygroscopic (LH, $0.1 \le \kappa < 0.2$), and more hygroscopic (MH, $\kappa \ge 0.2$). The MH groups mainly consist of inorganic species such as sulfates, nitrates, and ammonium salts. In contrast, the NH and LH groups are primarily composed of black carbon, insoluble organics, and partially soluble organics (Liu et al., 2011; Müller et al., 2017; Swietlicki et al., 2008).

The mean κ (κ_{mean}) is then defined as the number-weighted mean of κ-PDF over the κ range $[a, b]$:

$$\kappa_{mean} = \int_a^b \kappa\, c\,(\kappa, D_p)\,\mathrm{d}\kappa, \qquad (3)$$

where a and b represent the lower and upper integration limits of κ. For the ensemble κ_{mean}, the integral spans the entire domain, i.e., $a = 0$ and $b \rightarrow \infty$. When computing κ_{mean} of NH, LH, and MH hygroscopic groups (κ_{NH}, κ_{LH}, and κ_{MH}), a and b are set according to the predefined κ range of each group.

Accordingly, the number fraction (NF) for each hygroscopic group with over the range $[a, b]$ is defined as:

$$\text{NF} = \int_a^b c\,(\kappa, D_p)\,\mathrm{d}\kappa. \qquad (4)$$

The standard deviation of κ-PDF ($\sigma_{\kappa\text{-PDF}}$) is calculated as:

$$\sigma_{\kappa\text{-PDF}} = \left(\int_0^\infty (\kappa - \kappa_{mean})^2\, c\,(\kappa, D_p)\,\mathrm{d}\kappa\right)^{\frac{1}{2}}. \qquad (5)$$

Previous research has widely adopted $\sigma_{\kappa\text{-PDF}}$ as a metric for aerosol mixing state characterization (Jiang et al., 2016; Wang et al., 2017; Yuan et al., 2020). However, this absolute dispersion parameter fails to account for scenarios where significant κ_{mean} variations exist between different sizes. To address this limitation, this study introduces the coefficient of variation ($\text{CV}_{\kappa\text{-PDF}}$):

$$\text{CV}_{\kappa\text{-PDF}} = \frac{\sigma_{\kappa\text{-PDF}}}{\kappa_{mean}}. \qquad (6)$$

This parameter effectively captures the relative dispersion of size-resolved κ-PDF by incorporating κ_{mean} differences among particle populations. Consequently, $\text{CV}_{\kappa\text{-PDF}}$ serves as the primary mixing state indicator in this study, with lower values corresponding to stronger internal mixing.

2.2.2. Measurements of other aerosol properties

The measurement of aerosol chemical compositions is conducted using an aerosol chemical speciation monitor (ACSM, Aerodyne Research Inc.) coupled with an aethalometer (AE-33, Magee Scientific Inc.). Both instruments are configured with $PM_{2.5}$ sampling inlets: the ACSM system incorporates a $PM_{2.5}$ aerodynamic lens, while the AE-33 utilizes an aerosol cutter with 2.5 μm cutoff diameter. This configuration ensures measurement of particulate matter mass concentrations specifically for the aerodynamic diameter fraction below 2.5 μm ($PM_{2.5}$).

The ACSM operates at a temporal resolution of 15 minutes, while the AE-33 provides measurements at a higher resolution of 1 minutes. The ACSM, equipped with a capture vaporizer and a quadrupole mass spectrometer, is primarily used to measure the mass concentrations of organic aerosols (OA), sulfate (SO_4^{2-}), nitrate (NO_3^-), ammonium (NH_4^+), and chloride (Chl). To further analyse OA composition, the positive matrix factorization analysis is applied to differentiate between primary organic aerosols (POA) and secondary organic aerosols (SOA). Concurrently, the AE-33 is employed to measure the mass concentration of black carbon (BC). The total $PM_{2.5}$ mass concentration is derived by summing the mass concentrations of all components measured by the ACSM and AE-33. The absence of dust-related measurements may lead to underestimation of $PM_{2.5}$ mass concentrations during dust episodes in this study.

The particle number size distribution (PNSD) is measured by two scanning mobility particle sizers (SMPS) covering different size ranges: Nano-SMPS (2–60 nm) and SMPS (15–700 nm), both operating with a temporal resolution of 5 minutes. The PNSD-related data presented in this study are all provided by SMPS. NPF events are identified using SMPS data based on a significant particle number increase around 20 nm followed by banana-shaped PNSD growth, with nano-SMPS data being used auxiliarily for confirmation despite frequent gaps. Particles are classified into two modes based on their diameter: ultrafine mode ($D_p \leq 100$ nm) and accumulation mode (100 nm $< D_p \leq 700$ nm). Specifically, particles within the 40 nm $< D_p \leq 100$ nm range are classified as belonging to the Aitken mode. Then the total number concentrations in ultrafine- and accumulation-mode particles (N_{ult} and N_{acc}) are then calculated, separately.

2.3. Backward trajectory calculation and clustering analysis

Backward trajectories of air masses arriving at the sampling site are calculated using the NOAA HYSPLIT-4 (Hybrid Single-Particle Lagrangian Integrated Trajectory) model (Draxler and Hess, 1998; Wu et al., 2016). The 72-hour backward trajectories terminated at 100 m above ground level at 3-hour intervals from 00:00 to 21:00 LT (Local Time, UTC+08). The number of clusters is determined based on the variation in total spatial variance (refer to the HYSPLIT4 User Guide), with the k-means clustering algorithm applied to classify trajectories for each season. To balance optimal trajectory separation (favoring a larger number of clusters) with visualization simplicity (preferring fewer clusters), air mass backward trajectories are partitioned into 3 clusters per season.

3. Results and discussion

3.1. Overview

3.1.1. Seasonal variations of size-resolved aerosol hygroscopicity

As shown in Figure 1a, a significant increase in κ_{mean} with particle size is observed in all seasons, consistent with a previous study in Nanjing (Jiang et al., 2025). The size-resolved annual κ_{mean} values are 0.12 ± 0.04, 0.16 ± 0.05, 0.18 ± 0.05, 0.20 ± 0.05, and 0.22 ± 0.06 for particles with diameters of 40, 80, 110, 150, and 200 nm, respectively (Table S1). Similar hygroscopicity-particle size dependence is observed in Madrid, while more complex relationships are found in Athens, India and Switzerland (Alonso-Blanco et al., 2019; Kammermann et al., 2010; Ray et al., 2023; Spitieri et al., 2023). The enhancement of aerosol hygroscopicity with particle size may be attributed to chemical aging processes of particles and an increased proportion of inorganic components (Alonso-Blanco et al., 2019). Compared to the measurements in the NCP (Chen et al., 2022), κ at this site is relatively lower, likely due to the dominance of organic aerosols (annual average mass fraction: 42.92% in $PM_{2.5}$) (Figure 1b). This pattern closely resembles observations from Shanghai, which is also located within the YRD region (Chen et al., 2022).
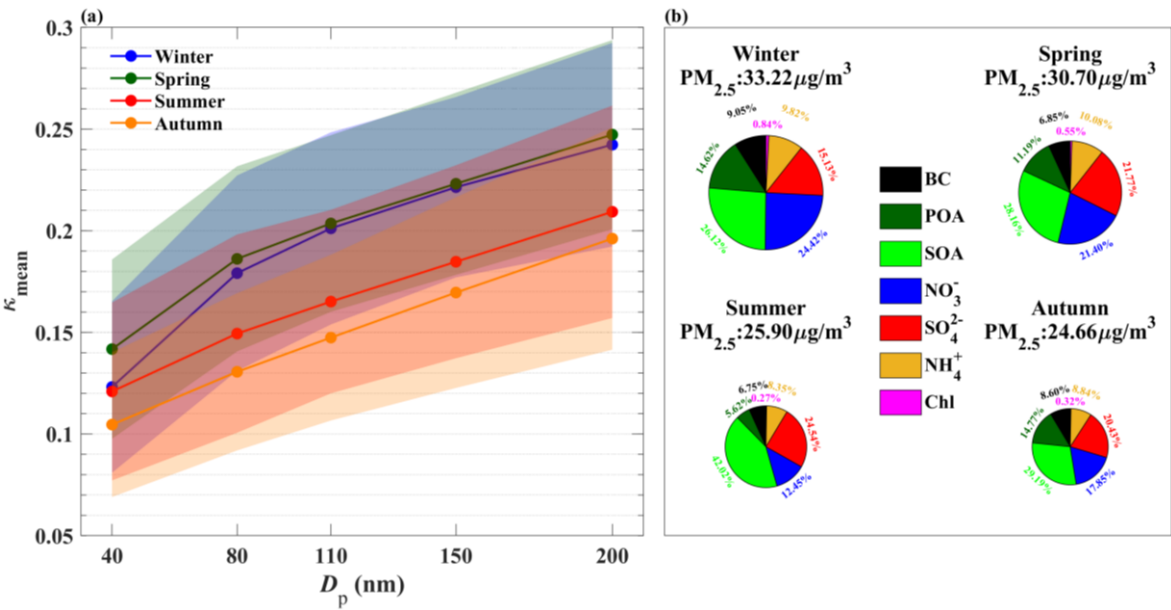
Figure 1. (a) Size variations of the mean hygroscopicity parameter (κ_{mean}) during different seasons, with error bands indicating the standard deviations of κ_{mean}. (b) Seasonal distributions of mass concentrations and compositional fractions for $PM_{2.5}$ chemical species.

A pronounced seasonal contrast in κ_{mean} is observed for 40 nm particles, with spring exhibiting the highest value ($\kappa_{mean} = 0.14$) compared to other seasons ($\kappa_{mean} = 0.10$–0.12). For larger particles (80–200 nm), obviously higher κ_{mean} values are recorded in winter and spring than in summer and autumn. This pattern may be attributed to the increased mass fractions of hydrophilic sulfate–nitrate–ammonium (SNA) during the more severe PM$_{2.5}$ pollution in winter and spring. As shown in Figure 1b, the mass concentrations of PM$_{2.5}$ during winter and spring exceed 30 μg m^{-3}, with corresponding relatively higher MF$_{SNA}$ (the mass concentration of SNA) values of 49.37% and 53.25%, respectively. In contrast, summer and autumn measurements show relatively lower PM$_{2.5}$ levels, averaging approximately 25 μg m^{-3}, with corresponding relatively lower MF$_{SNA}$ values of 45.34% and 47.12%, respectively. Similar seasonal variation patterns in aerosol chemical composition are reported at another site in Nanjing during 2016–2017 (Xie et al., 2022).

In summary, aerosols in the northern suburban area of Nanjing exhibit relatively low hygroscopicity, which may be mainly due to their relatively higher organic content. A consistent increase in hygroscopicity with particle size is observed across all seasons. Furthermore, aerosols in winter and spring demonstrate enhanced hygroscopicity in the 80–200 nm size range compared to summer and autumn, which can be attributed to relatively higher content of SNA.

3.1.2. Seasonal variations of hygroscopic groups in the different size particles

Figure 2a illustrates the seasonal variations in the NF and κ of different hygroscopic groups (NH, LH, MH) across various particle sizes. With the exception of 40 nm particles, the size variations in κ_{NH} and κ_{LH} are less pronounced than those of κ_{MH}. Meanwhile, compared with NF$_{NH}$ and NF$_{LH}$, NF$_{MH}$ shows a relatively obvious increase with particle size. Considering the increase of κ_{mean} with particle size (Figure 1a), this phenomenon suggests that the size variation in κ_{mean} may be mainly driven by MH group particles. Unlike particles in other size ranges, the 40 nm particles have relatively small seasonal differences in κ_{NH}, κ_{LH}, and κ_{MH}. The κ_{mean} of 40 nm particles in spring is relatively higher than in other seasons due to the lower NF$_{NH}$ and higher NF$_{MH}$ of 40 nm particles.

As shown in Figure 2a, for Aitken-mode particles, κ_{NH} is found to increase consistently from winter and spring to summer and autumn, whereas for accumulation-mode particles, the lowest κ_{NH} values are recorded during summer. However, the variation in κ_{NH} remains limited, generally within the range of 0.03–0.05. Furthermore, κ_{LH} for 40–150 nm particles is slightly higher in spring compared to other seasons, while for 200 nm particles, it reaches slightly higher values in summer. Despite these variations, the variation in κ_{LH} remains minor, typically ranging between 0.14–0.17, which is in the κ range of SOA (Petters and Kreidenweis, 2007). Across all particle sizes, both κ_{MH} and NF$_{MH}$ are bigger in winter and spring than in summer and autumn for the same particle sizes. Considering the higher κ_{mean} in winter and spring compared to summer and autumn (Figure 1a), this suggests that the seasonal in κ_{mean} is likely driven by MH group particles.

In general, aerosol particles exhibit higher κ_{MH} in winter than in spring, which may be attributed to the higher abundance of NO$_3^-$ in winter aerosols leading to enhanced hygroscopicity of MH groups. This effect is more pronounced in accumulation-mode particles compared to Aitken-mode particles, with κ_{MH} showing more distinct seasonal variations in the former. However, a relatively higher NF$_{MH}$ is observed in spring compared to winter due to the greater abundance of SNA, leading to a relatively

higher κ_{mean} in spring (Figure 1). Although the differences in aerosol κ_{MH} between summer and autumn are relatively small, the higher NF_{MH} in summer results in greater κ_{mean} across all particle size ranges compared to autumn.
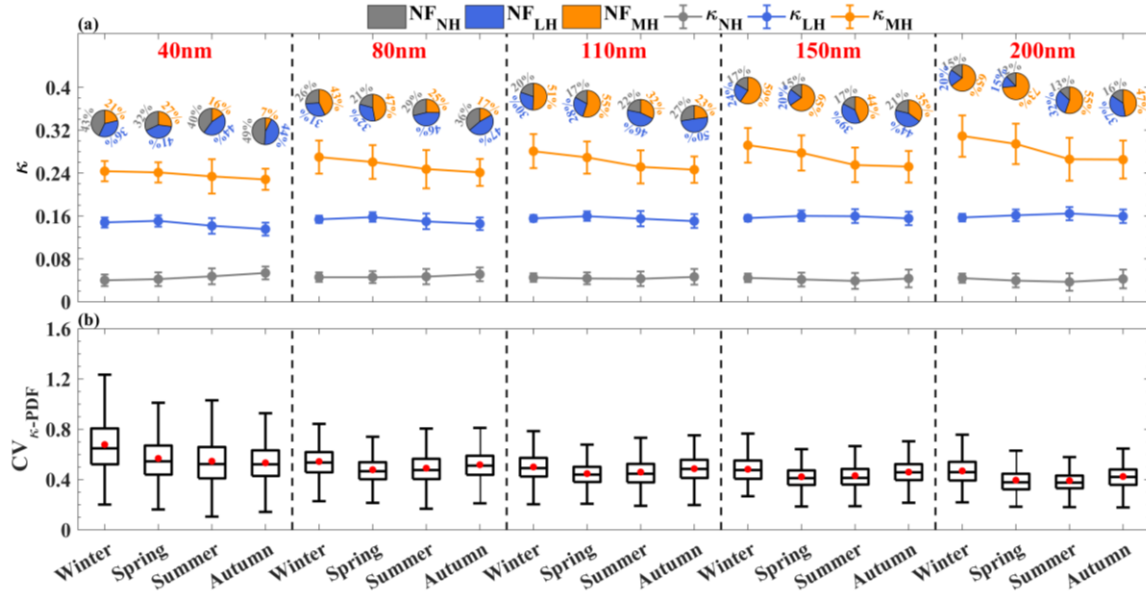
Figure 2. (a) Seasonal variations of NF_{MH}, NF_{LH}, and NF_{NH} (represented by orange, blue, and gray segments in the pie charts, respectively), alongside the corresponding κ_{MH}, κ_{LH}, and κ_{NH} (represented by orange, blue, and gray lines, respectively) for different size particles (40–200 nm). Error bars indicate the standard deviation of each parameter. (b) Seasonal variations of $CV_{\kappa\text{-PDF}}$ for different size particles. Boxplots display the mean (red dots), median (horizontal line), 25th and 75th percentiles (lower and upper box), and 5th and 95th percentiles (lower and upper whiskers).

As demonstrated in Figure 2b, the $CV_{\kappa\text{-PDF}}$ exhibits a decreasing trend with increasing particle size within the same season, reflecting enhanced internal mixing during aerosol aging from the Aitken mode to the accumulation mode. Notably, the $CV_{\kappa\text{-PDF}}$ values of particles in winter are relatively higher compared to other seasons, and this phenomenon is particularly evident for 40 nm particles. This indicates that, relative to other seasons, particles in winter exhibit a relatively pronounced external mixing state. This seasonal pattern likely results from reduced photochemical activity during winter months, which inhibits atmospheric aging processes and promotes the persistence of externally mixed aerosols.

To further elucidate the impact of different hygroscopic groups on κ_{mean}, the correlation coefficients (R^2) between the κ_{mean} and six parameters (NF_{MH}, NF_{LH}, NF_{NH}, κ_{MH}, κ_{LH}, and κ_{NH}) are calculated (Figure 3). The results indicate that κ_{mean} is predominantly influenced by NF_{MH} in all seasons, with the corresponding R^2 values all above 0.69. For Aitken-mode particles, κ_{mean} is also affected largely by NF_{NH}, particularly for 40 nm particles. In autumn, the R^2 between NF_{NH} and κ_{mean} ($R^2 = 0.77$) for 40 nm particles is even slightly higher than that between NF_{MH} and κ_{mean} ($R^2 = 0.71$). This phenomenon may be attributed to the fact that Aitken-mode particles, primarily originating from direct emissions or NPF events with limited aging, are typically

composed of more hydrophobic matters (e.g., OA and BC) (Gysel et al., 2007; Li et al., 2023). These particles are characterized by higher NF_{NH} and lower NF_{MH}, leading in an amplified influence of NF_{NH} on the κ_{mean} of Aitken-mode particles.
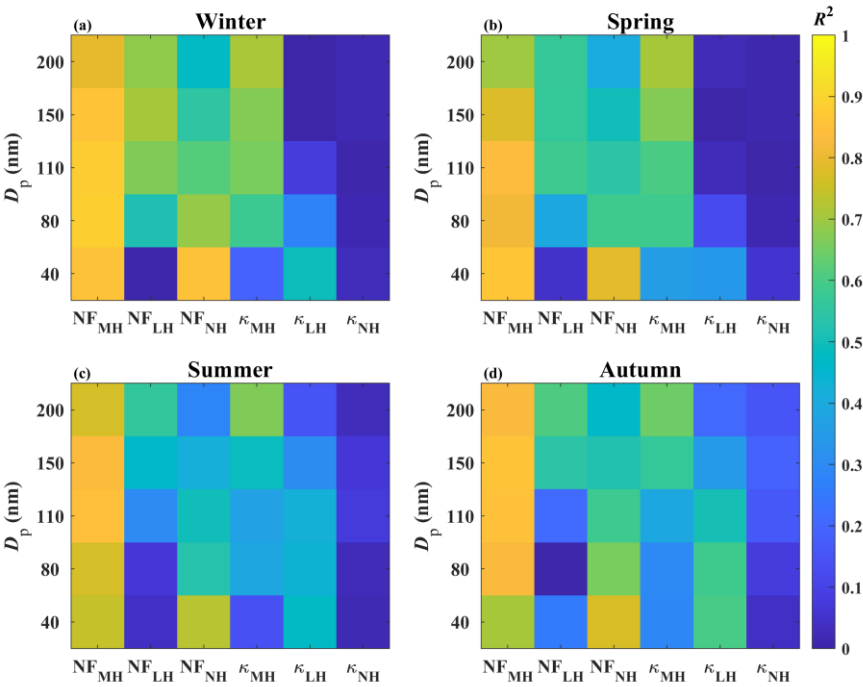
Figure 3. The correlation coefficients (R^2) between κ_{mean} and six parameters (NF_{MH}, NF_{LH}, NF_{NH}, κ_{MH}, κ_{LH}, κ_{NH}) for different size particles (40–200 nm) during different seasons.

Overall, these findings suggest that variations in the NF of different hygroscopic groups have a greater impact on κ_{mean} than variations in the κ values of these groups. Beyond the influence by the NF of different hygroscopic groups, κ_{mean} for relatively larger particles is also affected by κ_{MH}, while for relatively smaller particles, due to their relatively weaker hygroscopicity, κ_{mean} is jointly influenced by κ_{MH} and κ_{LH}. Compared to winter and spring, the influence of κ_{MH} on κ_{mean} is smaller in summer and autumn, whereas the influence of κ_{LH} on κ_{mean} is greater. This pattern is attributed to the κ_{mean} for the same particle sizes is lower in summer and autumn than in winter and spring.

3.1.3. Seasonal variation of diurnal cycles in aerosol hygroscopicity

As illustrated in Figure 4a1–a4, rush-hour-induced enhancements of particle number concentration demonstrate distinct seasonal variability, with pronounced effects on ultrafine-mode particles during morning (~06:00 LT) and evening (~20:00 LT) periods. This phenomenon is most pronounced in winter and spring, which may be related to the relatively stagnant

meteorological conditions during these seasons. Quantitative analysis reveals relatively obvious PM$_{2.5}$ mass accumulation during rush hours across all non-summer seasons, accompanied by synchronous increases in both BC mass concentrations and fractions (M_{BC} and MF$_{BC}$) (Figure 4). Relative to ultrafine-mode particles, the number concentration of accumulation-mode particles has a greater impact on PM$_{2.5}$ mass concentration. In contrast to other seasons, summer noon shows a more noticeable increasing trend in the number concentration of accumulation-mode particles, which to some extent weakens the diurnal variation amplitude of PM$_{2.5}$ mass concentration in summer, resulting in less pronounced changes in PM$_{2.5}$ mass concentration during summer rush hours (Figure 4c3). Traffic-related compositional changes during rush hours, especially increased NF$_{NH}$, systematically reduce κ_{mean} across most particle size ranges, with magnitudes varying by particle size and season (Figure 5). Compared to the Nanjing site in this study, sites like Madrid and Budapest show a more pronounced decline in κ_{mean} during traffic emissions rush hours (Alonso-Blanco et al., 2019; Enroth et al., 2018). This disparity implies that aerosol hygroscopicity at the Nanjing site is less sensitive to rush-hour traffic emissions. Notably, while PM$_{2.5}$ mass concentration increases are less significant during summer rush hours than in other seasons (Figure 4c3), the reductions in κ values across most particle size ranges are more pronounced. This observation likely stems from the relatively low total particle number concentration (N_{tot}) in summer, whereby traffic emissions during morning and evening rush hours represent a larger proportion of N_{tot}, thereby inducing a relatively pronounced decrease in κ_{mean}.
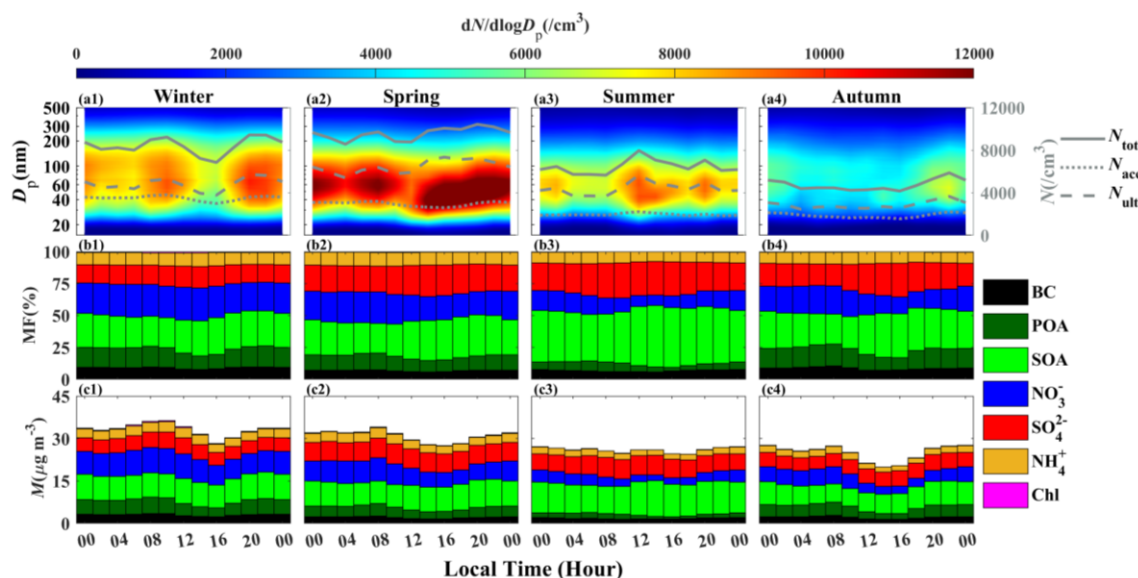
Figure 4. Diurnal variations of (a1–a4) particle number size distributions (PNSD), total particle number concentration (N_{tot}), accumulation-mode particle number concentration (N_{acc}), and ultrafine-mode particle number concentration (N_{ult}), (b1–b4) mass fractions (MF) of aerosol chemical species, and (c1–c4) mass concentrations (M) of aerosol chemical species during different seasons.
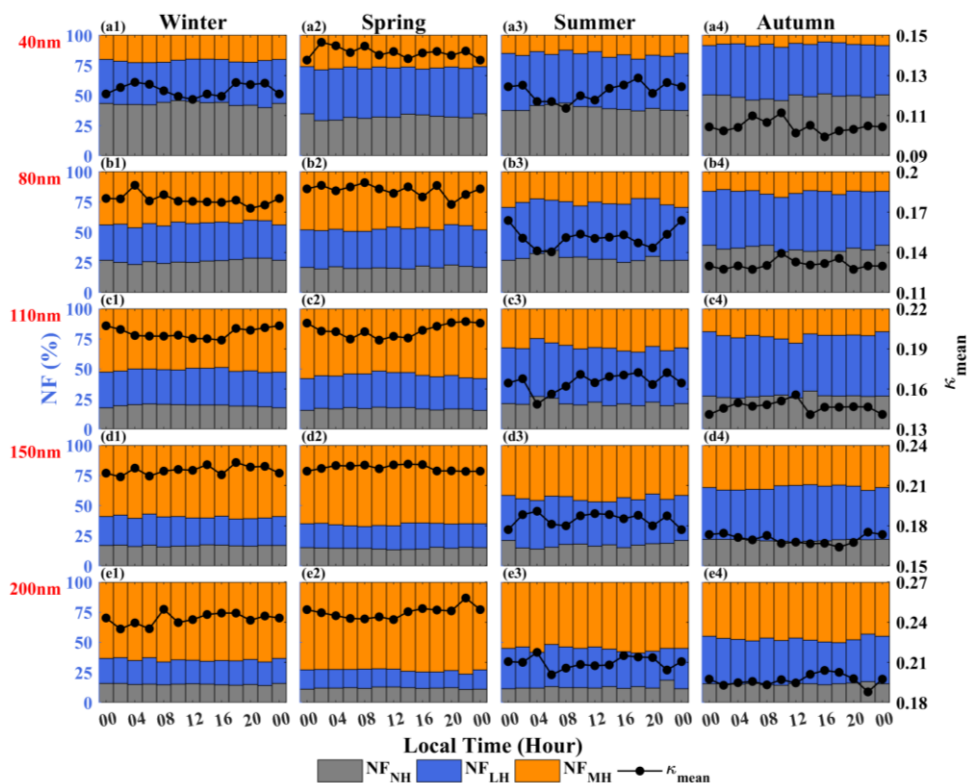
Figure 5. Diurnal variations of the NF_{MH} (orange bars), NF_{LH} (blue bars), and NF_{NH} (gray bars), and κ_{mean} (black dots) for different size particles (40–200 nm) during different seasons.

Figure 4b1–b4 reveals daytime increasing trend in the mass fractions of SO_4^{2-} and SOA mass fractions across all seasons, with peak values coinciding with periods of maximum photochemical activity—a trend most pronounced in summer due to enhanced solar radiation (Peng et al., 2017). In contrast, the mass fraction of NO_3^- displays an inverse diurnal cycle during non-winter periods, reaching maximal mass fractions during nocturnal periods. This behavior may stem from lower nocturnal temperatures and higher RH, which promote efficient aqueous-phase reactions and gas-particle partitioning, potentially involving NO_3 radical chemistry, converting gaseous precursors like NO_x into particulate NO_3^- (Sun et al., 2013). These compositional shifts drive distinct hygroscopicity dynamics primarily in accumulation-mode particles (e.g., 200 nm), as their composition aligns more closely with bulk $PM_{2.5}$ measurements (Wang et al., 2019). As shown in Figure 5, during non-winter periods, variations in NF among hygroscopicity groups result in two chemically-distinct diurnal patterns for κ_{mean} in 200 nm particles: an afternoon enhancement (14:00–18:00 LT), likely driven by photochemical production of hydrophilic SO_4^{2-} and SOA, and a nighttime enhancement (post-20:00 LT), associated with NO_3^- accumulation under favorable nocturnal conditions. This pattern is less evident in winter, where stagnant meteorological conditions suppress pollutant dispersion, leading to consistently high NO_3^- levels and minimal diurnal variation in NO_3^- mass fraction (Figure 4).

3.2. Impact of NPF events on the size-resolved aerosol hygroscopicity

Figure 4a2 shows that the spring afternoon period exhibits unique particle dynamics, with the size distribution displaying a subtle banana-shaped diurnal pattern (more evident in event-specific examples like Fig. S1a1). This pattern is potentially linked to the frequent NPF events that occur in spring. The frequency of NPF occurrences reaching 21% during spring (approximately double the annual average), significantly higher than in other seasons (Table S2). Previous studies have shown that strong winds during prevalent spring dust episodes in China significantly scavenge fine particles, creating a cleaner environment conducive to NPF occurrence (Shen et al., 2023; Xu et al., 2022). In contrast to spring non-NPF days, the spring NPF days shows more pronounced diurnal fluctuations in the number concentration of ultrafine-mode particles and the mass concentration of $PM_{2.5}$ chemical compositions (Fig. S1). As shown in Fig. S1c1, around 10:00 LT in the spring NPF days, the mass concentration of $PM_{2.5}$ sharply decreases. Under these low pollution conditions, the lower condensation sink (CS) facilitates the onset of NPF events (Hong et al., 2023). This leads to a rapid increase in N_{ult} (Fig. S1a1).

In comparison to spring non-NPF days, MF_{OA} significantly increases in spring NPF days, with MF_{SOA} gradually increases over time. This trend starts at 10:00 LT and continues until 18:00 LT to the evening rush hours (Fig. S1b1). This suggests that spring NPF events may be predominantly driven by the formation of SOA. Additionally, in contrast to spring non-NPF days, a slightly lower κ_{mean} is observed for 40 nm particles (Fig. S2a1), suggesting that the Aitken-mode particles originating from NPF events exhibit lower hygroscopicity. This is related to a higher NF_{NH} and a lower NF_{MH} (Fig. S2b1 and Fig. S2d1). As Aitken-mode particles grow during spring NPF days, the κ_{mean} of 40 nm particles shows a modest increase from 08:00 to 12:00 LT, while the κ_{mean} increase of 80 nm particles is relatively lagged from 10:00 to 14:00 LT (Fig. S2a1), though differences in κ_{mean} for 40 nm particles between NPF and non-NPF days are minimal due to their generally low and less variable values. Between 14:00–16:00 LT, the N_{ult} reaches its peak, while the N_{acc} and the $PM_{2.5}$ mass concentration reach their diurnal lows (Fig. S1). A slightly increasing trend in κ_{mean} occurs around 16:00 LT for most size particles, driven by concurrent increases in both the NF_{MH} and κ_{MH} (Figs. S2 and S3). This enhancement is particularly evident for accumulation-mode particles, which have a higher κ_{MH}. These findings suggest that Aitken-mode particles originating from NPF events, which exhibit lower hygroscopicity, gradually age and grow into more hygroscopic accumulation-mode particles over time during spring NPF days. As shown in Figure 6a, the κ_{NH}, κ_{LH} and κ_{MH} exhibit minimal difference between NPF days and non-NPF days during spring. However, the κ_{mean} on NPF days is significantly lower by 6.76% for 40 nm particles and higher by 5.07% for 200 nm particles compared to non-NPF days (Table S3). This divergence is attributed to the changes in the NF_{NH} and NF_{MH}: NPF days have larger NF_{NH} and smaller NF_{MH} for 40 nm particles, while the opposite is observed for 200 nm particles (Figure 6b). Additionally, the diurnal variation of $CV_{\kappa\text{-PDF}}$ for 40 nm particles in NPF days has relatively obvious fluctuation, while the $CV_{\kappa\text{-PDF}}$ for other particle sizes in NPF days and all particle sizes in non-NPF days has no obvious diurnal variation (Fig. S3a1–a4). This indicates that the NPF event may only have a relatively pronounced effect on the internal mixing state of 40 nm particles. Furthermore, the $CV_{\kappa\text{-PDF}}$ for Aitken-mode particles on NPF days is slightly larger than on non-NPF days, while the opposite is observed for accumulation-mode particles (Table S3). These findings suggest that, compared to non-NPF days, the internal mixing of

340 relatively smaller particles is slightly weakened on NPF days, while relatively larger particles exhibit a slightly enhanced state of internal mixing.
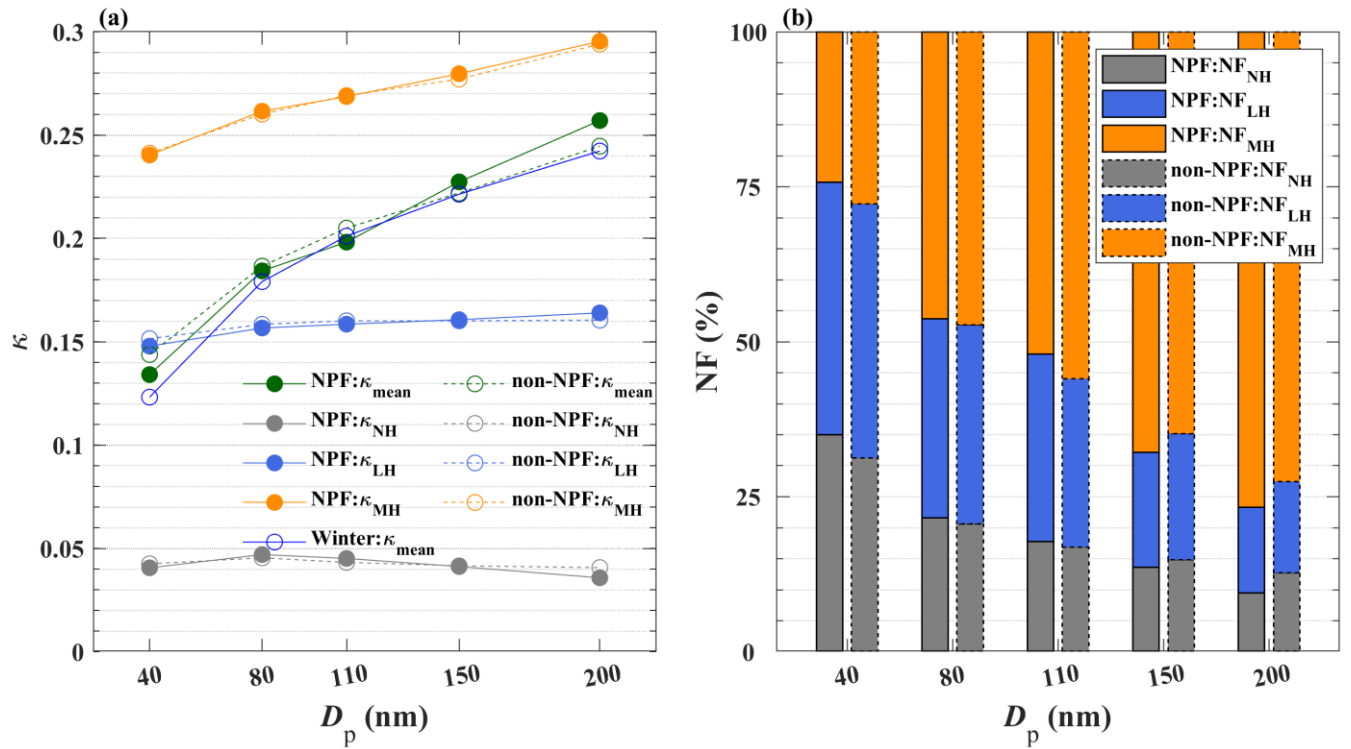
Figure 6. (a) κ_{mean}, κ_{MH}, κ_{LH} and κ_{NH} in spring NPF days and spring non-NPF days, and the κ_{mean} in winter for all size particles (40–200 nm). (b) NF_{MH}, NF_{LH}, NF_{NH} in spring NPF days and spring non-NPF days for all size particles (40–200 nm).

345 Similar to spring, winter exhibits the relatively higher κ_{mean} values for particles in the 40-200 nm size range compared to summer and autumn (Figure 1a). To further investigate seasonal differences, the κ_{mean} values of spring NPF days and non-NPF days are compared with winter conditions (Figure 6a). For Aitken-mode particles, winter consistently shows lower κ_{mean} values than both spring NPF and non-NPF days. For accumulation-mode particles (except for 110 nm), winter κ_{mean} values are significantly lower than spring NPF days but comparable to spring non-NPF days, with only a slight lower in κ_{mean} relative to
350 spring non-NPF days. Particles with a diameter of 110 nm represent a transitional size between the Aitken and accumulation modes. Their hygroscopicity in winter is slightly higher than that observed during spring NPF days, but slightly lower than during spring non-NPF days. These findings collectively demonstrate that, compared to spring non-NPF days, spring NPF days exhibit slightly reduced hygroscopicity in Aitken-mode particles and slightly enhanced hygroscopicity in accumulation-mode particles. Regardless of the influence of NPF events, particles of all sizes in spring demonstrate relatively stronger
355 hygroscopicity than those of the same size in other seasons, except for 110 nm particles, which show slightly lower hygroscopicity during spring NPF days compared to winter.

3.3. Impact of regional transport on aerosol hygroscopicity

3.3.1. Seasonal impacts of regional transport on aerosol hygroscopicity

Under the influence of the subtropical monsoon, seasonal variations in air mass sources are evident: while summer air masses derive from southern areas, other seasons primarily receive air masses from the northern region (Figure 7). Aerosol chemical composition analysis in different clusters shows that summer air masses contain substantially higher proportions of SOA in $PM_{2.5}$ compared to other seasons (Fig. S4). This compositional difference leads to elevated NF_{LH} values in summer, resulting in significantly lower κ_{mean} values for accumulation-mode particles relative to winter and spring (Figure 8).

In contrast, autumn air masses exhibit higher POA content in $PM_{2.5}$ (Fig. S4), yielding relatively increased NF_{NH} and NF_{LH} compared to summer conditions, along with slightly lower κ_{mean} values for equivalent particle sizes (Figure 8). While winter air masses demonstrate higher κ_{MH} (Fig. S5), spring air masses contain greater amounts of SNA in $PM_{2.5}$ (Fig. S4) and the elevated NF_{MH} ultimately produces slightly higher κ_{mean} values compared to that in winter (Figure 8). Collectively, these observations reveal that similar particle hygroscopicity under winter–spring air masses, and comparable hygroscopic properties under summer–autumn air masses (Figure 8).

As illustrated in Fig. S4, the size of the pie charts represents the $PM_{2.5}$ mass concentration in different clusters. Notably, springtime $PM_{2.5}$ mass concentrations show significant variation among air mass categories, with C2 exhibiting relatively lower mass concentrations than C1 and C3. As indicated in Table S4, the occurrence frequencies of NPF events during spring for C1, C2, and C3 are 11%, 42%, and 25%, respectively, suggesting that NPF events in Nanjing spring are more likely under the cleaner conditions of C2, characterized by lower $PM_{2.5}$ mass concentrations. This pattern may stem from reduced condensation sinks and higher abundances of gaseous precursors favorable for NPF in northerly air masses (Gysel et al., 2007; Li et al., 2023).
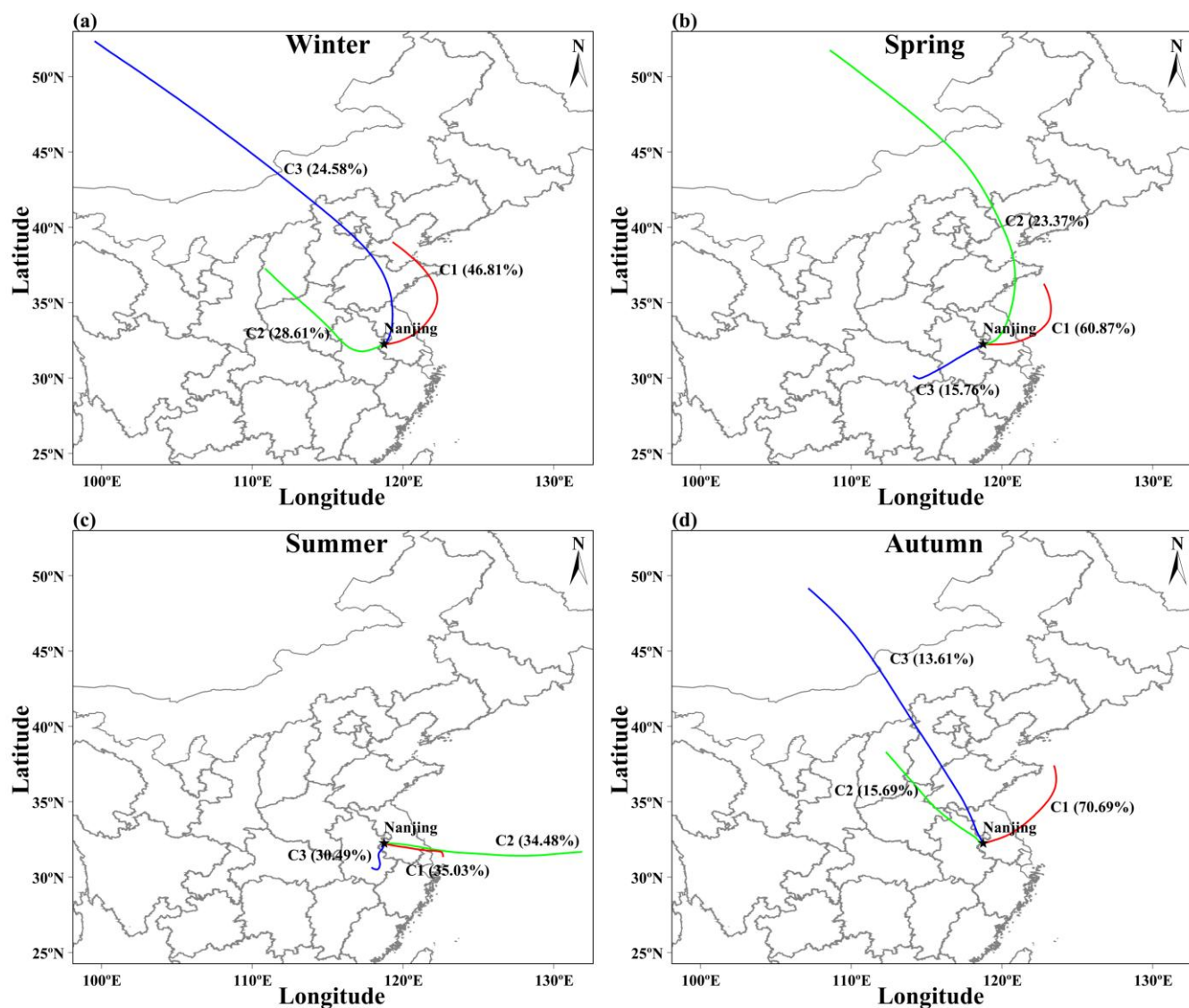
Figure 7. 72-hour air mass backward trajectories at a height of 100 meters corresponding to the cluster analysis during different seasons. The line colors denote different clusters, i.e., red for Cluster C1, green for Cluster C2, and blue for Cluster C3.

380
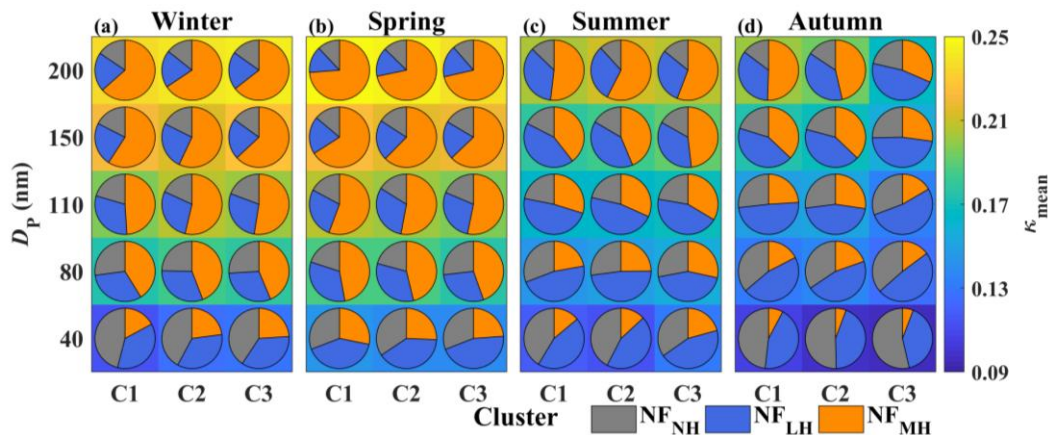
Figure 8. The κ_{mean} (color block) of aerosols and the number fractions of different hygroscopic groups for all size particles (40–200 nm) in the influence of different air masses during different seasons. The color blocks of pie chart denote number fractions of different hygroscopic groups, i.e., orange block of pie chart for NF_{MH}, blue block of pie chart for NF_{LH}, and gray block of pie chart for NF_{NH}.

3.3.2. Influence of regional transport on hygroscopicity of particles of different sizes

Across all seasons except autumn, 200 nm particles exhibit relatively weak variation in κ_{mean} across clusters. This phenomenon is due to relatively small differences in both NF of different hygroscopicity groups and κ_{MH} across clusters within the same season (Figure 8 and S5). In contrast, 200 nm particles during autumn display relatively large κ_{mean} variations across clusters, attributable to relatively larger differences in NF of different hygroscopicity groups despite comparable κ_{MH} values between air masses. These findings suggest that for 200 nm particles, NF of different hygroscopicity groups serves as the dominant factor governing κ_{mean}, a conclusion that aligns with the results presented in Sect.3.1.2.

Integrative examination of Figs. Figure 7, Figure 8, and S4 further reveals that, within a given season, 200 nm particles originating from eastern/northern air masses consistently exhibit stronger hygroscopicity compared to those from western/southern sources. This enhanced hygroscopic behavior can be attributed to their higher SNA content in $PM_{2.5}$. This phenomenon also exists to some extent in accumulation-mode particles of other sizes, except during summer.

For 40 nm particles, κ_{mean} is predominantly influenced by NF_{NH} and NF_{MH} (Figure 3), with NF_{NH} being relatively higher and NF_{MH} lower, particularly in autumn. Given that κ_{NH} remains relatively small and stable, seasonal variations in κ_{mean} are negligible despite relatively obvious NF_{NH} differences across air masses (Figure 8). This implies that the hygroscopicity of 40 nm particles is less sensitive to air mass origins and may be primarily regulated by local sources. However, an exception occurs in spring, where air masses yield relatively higher κ_{mean} values for 40 nm particles, a consequence of their relatively elevated NF_{MH} (Figure 8). However, for 80 nm particles, which are also in the Aitken mode but closer in size to the accumulation mode, the hygroscopicity differences influenced by air masses are similar to those of accumulation-mode particles and therefore are relatively significant across seasons (Figure 8).

Figure 9 shows the $CV_{\kappa\text{-PDF}}$ for size-resolved particles under varying air mass influences across seasons. Comparative analysis reveals that during non-summer seasons, 200 nm particles affected by long-range transported air masses (winter C3, spring C2, summer C2, autumn C3) demonstrate relatively higher $CV_{\kappa\text{-PDF}}$ values relative to other air masses, suggesting relatively pronounced external mixing. Interestingly, summer exhibits a distinct pattern where C2-influenced 200 nm particles show even relatively lower $CV_{\kappa\text{-PDF}}$ values compared to summer C1 and C3, indicating relatively advanced internal mixing. This seasonal anomaly may be attributed to enhanced photochemical aging during summer transport, driven by more intensive solar radiation. Consequently, while C2-associated 200 nm particles display marginally increased hygroscopicity during summer (Figure 8c), other seasons show no statistically discernible hygroscopicity enhancement in long-range transported particle clusters.
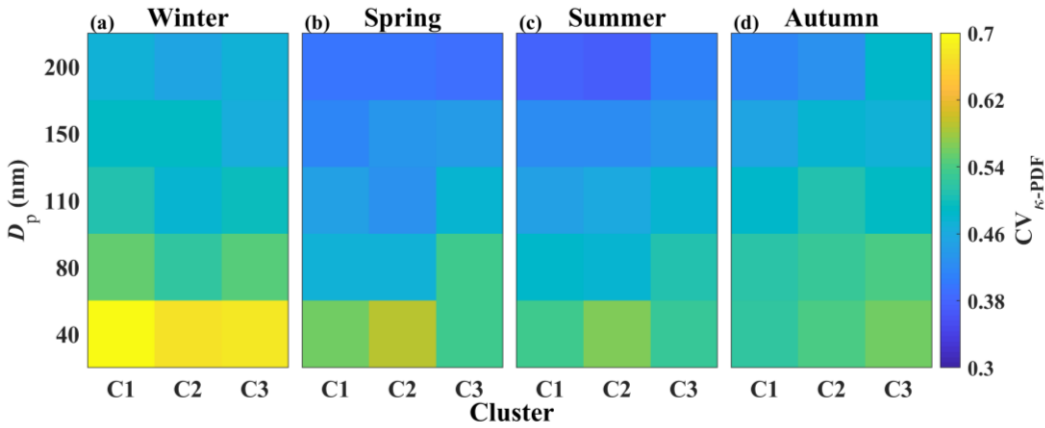
Figure 9. The $CV_{\kappa\text{-PDF}}$ for all size particles (40–200 nm) in the influence of different air masses during different seasons.

All these results reveal relatively smaller intra-seasonal variations in air mass hygroscopicity compared to inter-seasonal differences. This pattern primarily stems from relatively pronounced chemical composition disparities between seasonal air masses. The study demonstrates distinct spatial controls on particle hygroscopicity: 40 nm particles are likely predominantly influenced by local sources, as evidenced by relatively minimal κ_{mean} variations despite relatively obvious NF fluctuations. In contrast, within a given season, 200 nm particles originating from eastern/northern air masses display relatively enhanced hygroscopicity relative to their western/southern counterparts, attributable to relatively elevated SNA concentrations. Notably, long-range air mass transport induces hygroscopicity slight enhancement exclusively during summer months for 200 nm particles, a phenomenon driven by accelerated aging processes and relatively advanced internal mixing. No comparable effects are detected in other seasons.

4. Summary and conclusions

This study examines size-resolved and seasonal variations in aerosol hygroscopicity and their influencing factors in northern Nanjing, based on field observations at NUIST in 2021 using H-TDMA measurements.

Aerosols in this suburban region exhibit relatively low hygroscopicity, which may be mainly due to relatively higher organic content (annual average MF_{OA} in $PM_{2.5}$: 42.92%). The κ_{mean} increases with particle size across all seasons. Annual κ_{mean} values (± standard deviations) for 40, 80, 110, 150, and 200 nm particles are 0.12 ± 0.04, 0.16 ± 0.05, 0.18 ± 0.05, 0.20 ± 0.05, and 0.22 ± 0.06, respectively.

Winter and spring show relatively higher κ_{mean} as a result of the rise in MF_{SNA} under $PM_{2.5}$ pollution, which drives concurrent increases in both κ_{MH} and NF_{MH}. In contrast, summer and autumn exhibit relatively lower κ_{mean}. In winter, a high NO_3^- content boosts κ_{MH}, especially in accumulation-mode particles. However, κ_{mean} is highest in spring due to a relatively increased SNA content, which drives the enhancement of NF_{MH}. Notably, 40 nm particles in spring show the highest κ_{mean} due to both increased NF_{MH} and decreased NF_{NH}, although the seasonal differences in κ_{mean} for 40 nm particles during non-spring periods are relatively small.

Across all seasons, κ_{mean} is mainly governed by NF_{MH}. For relatively smaller particles, κ_{mean} is also influenced by NF_{NH}, κ_{MH}, and κ_{LH}—particularly at 40 nm—while relatively larger particles are more affected by κ_{MH}. In contrast to winter and spring, κ_{MH} 's influence diminishes relatively in summer and autumn, while that of κ_{LH} correspondingly increases. Photochemical processes increase SO_4^{2-} and SOA during daytime, while NO_3^- accumulates at night via aqueous-phase reactions (except winter). As a result, 200 nm particles show afternoon and evening κ_{mean} slight enhancement. Furthermore, traffic emissions cause κ_{mean} slightly dips across most sizes during morning and evening rush hours.

Spring records the highest frequency of new particle formation (NPF) events (21%). During these events, newly formed particles are likely organic-rich, leading to relatively lower κ_{mean} for 40 nm particles originating from NPF in the morning. With the aging of particles, the κ_{mean} for 200 nm particles slightly enhanced in the late afternoon. Compared to winter, Aitken-mode particles on spring NPF days and spring non-NPF days show relatively higher κ_{mean}, while accumulation-mode particles are similar on spring non-NPF days but relatively lower than spring NPF days (except for 110 nm). Compared to spring non-NPF days, κ_{mean} on spring NPF days decreases (by 6.76%) for 40 nm particles, and increases (by 5.07%) for 200 nm particles. Intra-seasonal variations in air mass hygroscopicity are relatively smaller than inter-seasonal differences, which may be attributed to the greater chemical contrast among seasonal air masses. Spatial controls differ by particle size: 40 nm particles may be primarily influenced by local sources, as indicated by relatively stable κ_{mean} despite NF variability. In contrast, within a given season, 200 nm particles transported from the east or north show relatively enhanced hygroscopicity due to higher SNA levels. Notably, long-range air mass transport enhances κ_{mean} for 200 nm particles only in summer, likely due to accelerated aging and more uniform internal mixing—an effect not observed in other seasons.

These findings provide valuable insights into the complex interactions between aerosol chemical composition, particle size, and seasonal-regional air mass transport in shaping aerosol hygroscopicity. Understanding these relationships is essential for

improving the accuracy of regional climate models, particularly in estimating aerosol–cloud interactions and radiative forcing. Moreover, the study highlights the critical role of local emissions and secondary processes in influencing aerosol properties, offering a scientific basis for air quality management and pollution control strategies in rapidly urbanizing regions like Nanjing and the broader Yangtze River Delta.

465

Data availability. Data used in the study are available from the corresponding author upon request (yuyingwang@nuist.edu.cn).

Author contributions. YW designed the experiment; JZ, JX and YW carried it out and analysed the data. Other co-authors participated in science discussions and suggested analyses. JZ and YW prepared the paper with contributions from all co-authors.

Competing interests. The authors declare that they have no conflict of interest.

Acknowledgements. This work is funded by National Natural Science Foundation of China (NSFC) research projects (Grant Nos. 42030606 and 42575093). We thank all participants in the field campaign for their tireless work and cooperation.

470

475

References:

Alonso-Blanco, E., Gómez-Moreno, F.J., and Artíñano, B.: Size-resolved hygroscopicity of ambient submicron particles in a suburban atmosphere, Atmos. Environ., 213, 349-358, https://doi.org/10.1016/j.atmosenv.2019.05.065, 2019.

Asmi, E., Frey, A., Virkkula, A., Ehn, M., Manninen, H.E., Timonen, H., Tolonen-Kivimäki, O., Aurela, M., Hillamo, R., and Kulmala, M.: Hygroscopicity and chemical composition of Antarctic sub-micrometre aerosol particles and observations of new particle formation, Atmos. Chem. Phys., 10, 4253-4271, https://doi.org/10.5194/acp-10-4253-2010, 2010.

Chen, J., Li, Z., Lv, M., Wang, Y., Wang, W., Zhang, Y., Wang, H., Yan, X., Sun, Y., and Cribb, M.: Aerosol hygroscopic growth, contributing factors, and impact on haze events in a severely polluted region in northern China, Atmos. Chem. Phys., 19, 1327-1342, https://doi.org/10.5194/acp-19-1327-2019, 2019.

Chen, L., Zhang, F., Zhang, D., Wang, X., Song, W., Liu, J., Ren, J., Jiang, S., Li, X., and Li, Z.: Measurement report: Hygroscopic growth of ambient fine particles measured at five sites in China, Atmos. Chem. Phys., 22, 6773-6786, https://doi.org/10.5194/acp-22-6773-2022, 2022.

Chen, Y., Wang, X., Dai, W., Wang, Q., Guo, X., Liu, Y., Qi, W., Shen, M., Zhang, Y., Li, L., Cao, Y., Wang, Y., and Li, J.: Particle Number Size Distribution of Wintertime Alpine Aerosols and Their Activation as Cloud Condensation Nuclei in the Guanzhong Plain, Northwest China, J. Geophys. Res.-Atmos., 128, e2022JD037877, https://doi.org/10.1029/2022JD037877, 2023.

Draxler, R. R. and Hess, G. D.: An overview of the HYSPLIT_4 modelling system for trajectories dispersion and deposition, Aust. Meteorol. Mag., 47, 295–308, 1998.

Enroth, J., Mikkilä, J., Németh, Z., Kulmala, M., and Salma, I.: Wintertime hygroscopicity and volatility of ambient urban aerosol particles, Atmos Chem Phys, 18, 4533-4548, https://doi.org/10.5194/acp-18-4533-2018, 2018.

Fan, X., Liu, J., Zhang, F., Chen, L., Collins, D., Xu, W., Jin, X., Ren, J., Wang, Y., Wu, H., Li, S., Sun, Y., and Li, Z.: Contrasting size-resolved hygroscopicity of fine particles derived by HTDMA and HR-ToF-AMS measurements between summer and winter in Beijing: the impacts of aerosol aging and local emissions, Atmos. Chem. Phys., 20, 915-929, https://doi.org/10.5194/acp-20-915-2020, 2020.

Fors, E.O., Swietlicki, E., Svenningsson, B., Kristensson, A., Frank, G.P., and Sporre, M.: Hygroscopic properties of the ambient aerosol in southern Sweden – a two year study, Atmos. Chem. Phys., 11, 8343-8361, https://doi.org/10.5194/acp-11-8343-2011, 2011.

Gysel, M., Crosier, J., Topping, D.O., Whitehead, J.D., Bower, K.N., Cubison, M.J., Williams, P.I., Flynn, M.J., McFiggans, G.B., and Coe, H.: Closure study between chemical composition and hygroscopic growth of aerosol particles during TORCH2, Atmos. Chem. Phys., 7, 6131-6144, https://doi.org/10.5194/acp-7-6131-2007, 2007.

Hirshorn, N.S., Zuromski, L.M., Rapp, C., McCubbin, I., Carrillo-Cardenas, G., Yu, F., and Hallar, A.G.: Seasonal significance of new particle formation impacts on cloud condensation nuclei at a mountaintop location, Atmos. Chem. Phys., 22, 15909-15924, https://doi.org/10.5194/acp-22-15909-2022, 2022.

Hong, J., Ma, J., Ma, N., Shi, J., Xu, W., Zhang, G., Zhu, S., Zhang, S., Tang, M., Pan, X., Xie, L., Li, G., Kuhn, U., Yan, C., Qi, X., Zha, Q., Nie, W., Tao, J., He, Y., Zhou, Y., Sun, Y., Xu, H., Liu, L., Cai, R., Zhou, G., Kuang, Y., Yuan, B., Wang, Q., Petäjä, T., Kerminen, V., Kulmala, M., Cheng, Y., and Su, H.: Low Hygroscopicity of Newly Formed Particles on the North China Plain and Its Implications for Nanoparticle Growth, Geophys. Res. Lett., 51, e2023GL107516, https://doi.org/10.1029/2023GL107516, 2024.

Hong, J., Tang, M., Wang, Q., Ma, N., Zhu, S., Zhang, S., Pan, X., Xie, L., Li, G., Kuhn, U., Yan, C., Tao, J., Kuang, Y., He, Y., Xu, W., Cai, R., Zhou, Y., Wang, Z., Zhou, G., Yuan, B., Cheng, Y., and Su, H.: Measurement Report: Wintertime new particle formation in the rural area of the North China Plain – influencing factors and possible formation mechanism, Atmos. Chem. Phys., 23, 5699-5713, https://doi.org/10.5194/acp-23-5699-2023, 2023.

Jiang, R., Tan, H., Tang, L., Cai, M., Yin, Y., Li, F., Liu, L., Xu, H., Chan, P.W., Deng, X., and Wu, D.: Comparison of aerosol hygroscopicity and mixing state between winter and summer seasons in Pearl River Delta region, China, Atmos. Res., 169, 160-170, https://doi.org/10.1016/j.atmosres.2015.09.031, 2016.

Jiang, Y., Ma, Y., Zheng, J., Ye, N., and Yuan, C.: Characterization of size-resolved aerosol hygroscopicity and liquid water content in Nanjing of the Yangtze River Delta, J. Environ. Sci., 151, 26-41, https://doi.org/10.1016/j.jes.2024.03.035, 2025.

Jin, X., Li, Z., Wu, T., Wang, Y., Su, T., Ren, R., Wu, H., Zhang, D., Li, S., and Cribb, M.: Differentiating the Contributions of Particle Concentration, Humidity, and Hygroscopicity to Aerosol Light Scattering at Three Sites in China, J. Geophys. Res.-Atmos., 127, e2022JD036891, https://doi.org/10.1029/2022JD036891, 2022.

Kammermann, L., Gysel, M., Weingartner, E., and Baltensperger, U.: 13-month climatology of the aerosol hygroscopicity at the free tropospheric site Jungfraujoch (3580 m a.s.l.), Atmos. Chem. Phys., 10, 10717-10732, https://doi.org/10.5194/acp-10-10717-2010, 2010.

Li, X., Chen, Y., Li, Y., Cai, R., Li, Y., Deng, C., Wu, J., Yan, C., Cheng, H., Liu, Y., Kulmala, M., Hao, J., Smith, J.N., and Jiang, J.: Seasonal variations in composition and sources of atmospheric ultrafine particles in urban Beijing based on near-continuous measurements, Atmos. Chem. Phys., 23, 14801-14812, https://doi.org/10.5194/acp-23-14801-2023, 2023.

Liu, J., Zhang, F., Xu, W., Sun, Y., Chen, L., Li, S., Ren, J., Hu, B., Wu, H., and Zhang, R.: Hygroscopicity of Organic Aerosols Linked to Formation Mechanisms, Geophys. Res. Lett., 48, e2020GL091683, https://doi.org/10.1029/2020GL091683, 2021.

Liu, N., Cui, S., Luo, T., Chen, S., Yang, K., Ma, X., Sun, G., and Li, X.: Characteristics of Aerosol Extinction Hygroscopic Growth in the Typical Coastal City of Qingdao, China, Remote Sens., 14, 6288, https://doi.org/10.3390/rs14246288, 2022.

Liu, P.F., Zhao, C.S., Göbel, T., Hallbauer, E., Nowak, A., Ran, L., Xu, W.Y., Deng, Z.Z., Ma, N., Mildenberger, K., Henning, S., Stratmann, F., and Wiedensohler, A.: Hygroscopic properties of aerosol particles at high relative humidity and their diurnal variations in the North China Plain, Atmos. Chem. Phys., 11, 3479-3494, https://doi.org/10.5194/acp-11-3479-2011, 2011.

Ma, N., Zhao, C., Tao, J., Wu, Z., Kecorius, S., Wang, Z., Größ, J., Liu, H., Bian, Y., Kuang, Y., Teich, M., Spindler, G., Müller, K., van Pinxteren, D., Herrmann, H., Hu, M., and Wiedensohler, A.: Variation of CCN activity during new particle

formation events in the North China Plain, Atmos. Chem. Phys., 16, 8593-8607, https://doi.org/10.5194/acp-16-8593-2016, 2016.

Mamali, D., Mikkilä, J., Henzing, B., Spoor, R., Ehn, M., Petäjä, T., Russchenberg, H., and Biskos, G.: Long-term observations of the background aerosol at Cabauw, The Netherlands, Sci. Total Environ., 625, 752-761, https://doi.org/10.1016/j.scitotenv.2017.12.136, 2018.

Müller, A., Miyazaki, Y., Aggarwal, S.G., Kitamori, Y., Boreddy, S.K.R., and Kawamura, K.: Effects of chemical composition and mixing state on size-resolved hygroscopicity and cloud condensation nuclei activity of submicron aerosols at a suburban site in northern Japan in summer, J. Geophys. Res.-Atmos., 122, 9301-9318, https://doi.org/10.1002/2017JD027286, 2017.

Peng, C., Wang, Y., Wu, Z., Chen, L., Huang, R.J., Wang, W., Wang, Z., Hu, W., Zhang, G., Ge, M., Hu, M., Wang, X., and Tang, M.: Tropospheric aerosol hygroscopicity in China, Atmos. Chem. Phys., 20, 13877-13903, https://doi.org/10.5194/acp-20-13877-2020, 2020.

Peng, J., Hu, M., Du, Z., Wang, Y., Zheng, J., Zhang, W., Yang, Y., Qin, Y., Zheng, R., Xiao, Y., Wu, Y., Lu, S., Wu, Z., Guo, S., Mao, H., and Shuai, S.: Gasoline aromatics: a critical determinant of urban secondary organic aerosol formation, Atmos. Chem. Phys., 17, 10743-10752, https://doi.org/10.5194/acp-17-10743-2017, 2017.

Petters, M.D., and Kreidenweis, S.M.: A single parameter representation of hygroscopic growth and cloud condensation nucleus activity, Atmos. Chem. Phys., 7, 1961-1971, https://doi.org/10.5194/acp-7-1961-2007, 2007.

Ray, A., Pandithurai, G., Mukherjee, S., Kumar, V.A., Hazra, A., Patil, R.D., and Waghmare, V.: Seasonal variability in size-resolved hygroscopicity of sub-micron aerosols over the Western Ghats, India: Closure and parameterization, Sci. Total Environ., 869, 161753, https://doi.org/10.1016/j.scitotenv.2023.161753, 2023.

Rosenfeld, D., Sherwood, S., Wood, R., and Donner, L.: Climate Effects of Aerosol-Cloud Interactions, Science, 343, 379-380, https://doi.org/10.1126/science.1247490, 2014.

Shen, X., Sun, J., Che, H., Zhang, Y., Zhou, C., Gui, K., Xu, W., Liu, Q., Zhong, J., Xia, C., Hu, X., Zhang, S., Wang, J., Liu, S., Lu, J., Yu, A., and Zhang, X.: Characterization of dust-related new particle formation events based on long-term measurement in the North China Plain, Atmos. Chem. Phys., 23, 8241-8257, https://doi.org/10.5194/acp-23-8241-2023, 2023.

Shi, J., Hong, J., Ma, N., Luo, Q., He, Y., Xu, H., Tan, H., Wang, Q., Tao, J., Zhou, Y., Han, S., Peng, L., Xie, L., Zhou, G., Xu, W., Sun, Y., Cheng, Y., and Su, H.: Measurement report: On the difference in aerosol hygroscopicity between high and low relative humidity conditions in the North China Plain, Atmos. Chem. Phys., 22, 4599-4613, https://doi.org/10.5194/acp-22-4599-2022, 2022.

Song, X., Wang, Y., Huang, X., Wang, Y., Li, Z., Zhu, B., Ren, R., An, J., Yan, J., Zhang, R., Shang, Y., and Zhan, P.: The Impacts of Dust Storms With Different Transport Pathways on Aerosol Chemical Compositions and Optical Hygroscopicity of Fine Particles in the Yangtze River Delta, J. Geophys. Res.-Atmos., 128, e2023JD039679, https://doi.org/10.1029/2023JD039679, 2023.

Spitieri, C., Gini, M., Gysel-Beer, M., and Eleftheriadis, K.: Annual cycle of hygroscopic properties and mixing state of the suburban aerosol in Athens, Greece, Atmos. Chem. Phys., 23, 235-249, https://doi.org/10.5194/acp-23-235-2023, 2023.

Sun, Y., Wang, Z., Fu, P., Jiang, Q., Yang, T., Li, J., and Ge, X.: The impact of relative humidity on aerosol composition and evolution processes during wintertime in Beijing, China, Atmos. Environ., 77, 927-934, https://doi.org/10.1016/j.atmosenv.2013.06.019, 2013.

Svenningsson, B., Rissler, J., Swietlicki, E., Mircea, M., Bilde, M., Facchini, M.C., Decesari, S., Fuzzi, S., Zhou, J., Mønster, J., and Rosenørn, T.: Hygroscopic growth and critical supersaturations for mixed aerosol particles of inorganic and organic compounds of atmospheric relevance, Atmos. Chem. Phys., 6, 1937-1952, https://doi.org/10.5194/acp-6-1937-2006, 2006.

Swietlicki, E., Hansson, H.C., Hämeri, K., Svenningsson, B., Massling, A., McFiggans, G., McMurry, P.H., Petäjä, T., Tunved, P., Gysel, M., Topping, D., Weingartner, E., Baltensperger, U., Rissler, J., Wiedensohler, A., and Kulmala, M.: Hygroscopic properties of submicrometer atmospheric aerosol particles measured with H-TDMA instruments in various environments - a review, Tellus B, 60, 432-469, https://doi.org/10.1111/j.1600-0889.2008.00350.x, 2008.

Swietlicki, E., Zhou, J., Berg, O.H., Martinsson, B.G., Frank, G., Cederfelt, S., Dusek, U., Berner, A., Birmili, W., Wiedensohler, A., Yuskiewicz, B., and Bower, K.N.: A closure study of sub-micrometer aerosol particle hygroscopic behaviour, Atmos. Res., 50, 205-240, https://doi.org/10.1016/S0169-8095(98)00105-7, 1999.

Tan, H., Yin, Y., Gu, X., Li, F., Chan, P.W., Xu, H., Deng, X., and Wan, Q.: An observational study of the hygroscopic properties of aerosols over the Pearl River Delta region, Atmos. Environ., 77, 817-826, https://doi.org/10.1016/j.atmosenv.2013.05.049, 2013.

Wang, H., An, J., Cheng, M., Shen, L., Zhu, B., Li, Y., Wang, Y., Duan, Q., Sullivan, A., and Xia, L.: One year online measurements of water-soluble ions at the industrially polluted town of Nanjing, China: Sources, seasonal and diurnal variations, Chemosphere, 148, 526-536, https://doi.org/10.1016/j.chemosphere.2016.01.066, 2016.

Wang, N., Wang, Y., Lu, C., Zhu, B., Yan, X., Sun, Y., Xu, J., Zhang, J., and Shen, Z.: Interpretable ensemble learning unveils main aerosol optical properties in predicting cloud condensation nuclei number concentration, Npj Clim Atmos Sci, 8, 302, https://doi.org/10.1038/s41612-025-01181-y, 2025.

Wang, X., Shen, X.J., Sun, J.Y., Zhang, X.Y., Wang, Y.Q., Zhang, Y.M., Wang, P., Xia, C., Qi, X.F., and Zhong, J.T.: Size-resolved hygroscopic behavior of atmospheric aerosols during heavy aerosol pollution episodes in Beijing in December 2016, Atmos. Environ., 194, 188-197, https://doi.org/10.1016/j.atmosenv.2018.09.041, 2018.

Wang, Y., Li, Z., Zhang, R., Jin, X., Xu, W., Fan, X., Wu, H., Zhang, F., Sun, Y., Wang, Q., Cribb, M., and Hu, D.: Distinct Ultrafine- and Accumulation-Mode Particle Properties in Clean and Polluted Urban Environments, Geophys. Res. Lett., 46, 10918-10925, https://doi.org/10.1029/2019GL084047, 2019.

Wang, Y., Li, Z., Zhang, Y., Du, W., Zhang, F., Tan, H., Xu, H., Fan, T., Jin, X., Fan, X., Dong, Z., Wang, Q., and Sun, Y.: Characterization of aerosol hygroscopicity, mixing state, and CCN activity at a suburban site in the central North China Plain, Atmos. Chem. Phys., 18, 11739-11752, https://doi.org/10.5194/acp-18-11739-2018, 2018.

Wang, Y., Zhang, F., Li, Z., Tan, H., Xu, H., Ren, J., Zhao, J., Du, W., and Sun, Y.: Enhanced hydrophobicity and volatility of submicron aerosols under severe emission control conditions in Beijing, Atmos. Chem. Phys., 17, 5239-5251, https://doi.org/10.5194/acp-17-5239-2017, 2017.

Wang, Y., Zhang, R., Wang, N., Xu, J., Zhang, J., Cui, C., Lu, C., Zhu, B., Sun, Y., and Zhu, Y.: The Role of Relative Humidity in Estimating Cloud Condensation Nuclei Number Concentration Through Aerosol Optical Data: Mechanisms and Parameterization Strategies, Geophys. Res. Lett., 52, e2024GL112734, https://doi.org/10.1029/2024GL112734, 2025.

615 Wu, Z.J., Zheng, J., Shang, D.J., Du, Z.F., Wu, Y.S., Zeng, L.M., Wiedensohler, A., and Hu, M.: Particle hygroscopicity and its link to chemical composition in the urban atmosphere of Beijing, China, during summertime, Atmos. Chem. Phys., 16, 1123-1138, https://doi.org/10.5194/acp-16-1123-2016, 2016.

Xie, M., Feng, W., He, S., and Wang, Q.: Seasonal variations, temperature dependence, and sources of size-resolved PM components in Nanjing, east China, J. Environ. Sci., 121, 175-186, https://doi.org/10.1016/j.jes.2021.12.022, 2022.

620 Xu, X., Zhao, P., Yin, Y., Cheng, W., Wang, J., Li, P., Liu, Y., Dai, J., and Yuan, W.: Dust particles transport during the rare strong sandstorm process in Northern China in early year 2021, Air Quality, Atmosphere & Health, 15, 929-936, https://doi.org/10.1007/s11869-022-01159-2, 2022.

Yang, Y., Li, Z., Guo, J., Wang, Y., Wu, H., Shang, Y., Wang, Y., Zhu, L., and Yan, X.: Revolutionizing Clear-Sky Humidity Profile Retrieval with Multi-Angle-Aware Networks for Ground-Based Microwave Radiometers, Journal of Remote Sensing, 625 5, 736, https://doi.org/10.34133/remotesensing.0736, 2025.

Yli-Juuti, T., Nieminen, T., Hirsikko, A., Aalto, P.P., Asmi, E., Hõrrak, U., Manninen, H.E., Patokoski, J., Dal Maso, M., Petäjä, T., Rinne, J., Kulmala, M., and Riipinen, I.: Growth rates of nucleation mode particles in Hyytiälä during 2003−2009: variation with particle size, season, data analysis method and ambient conditions, Atmos. Chem. Phys., 11, 12865-12886, https://doi.org/10.5194/acp-11-12865-2011, 2011.

630 Yuan, L., Zhang, X., Feng, M., Liu, X., Che, Y., Xu, H., Schaefer, K., Wang, S., and Zhou, Y.: Size-resolved hygroscopic behaviour and mixing state of submicron aerosols in a megacity of the Sichuan Basin during pollution and fireworks episodes, Atmos Environ, 226, 117393, https://doi.org/10.1016/j.atmosenv.2020.117393, 2020.

Zhang, F., Wang, Y., Peng, J., Ren, J., Collins, D., Zhang, R., Sun, Y., Yang, X., and Li, Z.: Uncertainty in Predicting CCN Activity of Aged and Primary Aerosols, J. Geophys. Res.-Atmos., 122, 11, 711-723, 736, 635 https://doi.org/10.1002/2017JD027058, 2017.

Zhang, S., Shen, X., Sun, J., Che, H., Zhang, Y., Liu, Q., Xia, C., Hu, X., Zhong, J., Wang, J., Liu, S., Lu, J., Yu, A., and Zhang, X.: Seasonal variation of particle hygroscopicity and its impact on cloud-condensation nucleus activation in the Beijing urban area, Atmos. Environ., 302, 119728, https://doi.org/10.1016/j.atmosenv.2023.119728, 2023.